

# Detectability of Decadal Anthropogenic Hydroclimate Changes over North America<sup>Ⓞ</sup>

HONGHAI ZHANG

*Program in Atmospheric and Oceanic Sciences, Princeton University, and NOAA/Geophysical Fluid Dynamical Laboratory, Princeton, New Jersey*

THOMAS L. DELWORTH

*NOAA/Geophysical Fluid Dynamical Laboratory, Princeton, New Jersey*

(Manuscript received 1 June 2017, in final form 15 December 2017)

## ABSTRACT

Regional hydroclimate changes on decadal time scales contain substantial natural variability. This presents a challenge for the detection of anthropogenically forced hydroclimate changes on these spatio-temporal scales because the signal of anthropogenic changes is modest, compared to the noise of natural variability. However, previous studies have shown that this signal-to-noise ratio can be greatly improved in a large model ensemble where each member contains the same signal but different noise. Here, using multiple state-of-the-art large ensembles from two climate models, the authors quantitatively assess the detectability of anthropogenically caused decadal shifts in precipitation-minus-evaporation (PmE) mean state against natural variability, focusing on North America during 2000–50. Anthropogenic forcing is projected to cause detectable (signal larger than noise) shifts in PmE mean state relative to the 1950–99 climatology over 50%–70% of North America by 2050. The earliest detectable signals include, during November–April, a moistening over northeastern North America and a drying over southwestern North America and, during May–October, a drying over central North America. Different processes are responsible for these signals. Changes in submonthly transient eddy moisture fluxes account for the northeastern moistening and central drying, while monthly atmospheric circulation changes explain the southwestern drying. These model findings suggest that despite the dominant role of natural internal variability on decadal time scales, anthropogenic shifts in PmE mean state can be detected over most of North America before the middle of the current century.

## 1. Introduction

The trajectory of Earth's climate system is determined by anthropogenic forcing and natural climate variability. Anthropogenic forcing comes from human activities, such as emissions of greenhouse gases and aerosols and changes in land use; natural climate variability consists of both forced variability by natural processes, such as volcanic eruptions and solar variations, and unforced variability arising from processes internal to land, ocean, atmosphere, and cryosphere, as well as their interactions. The unforced natural variability is often referred to as internal climate variability. The relative role of these

factors in the climate system varies with time and spatial scales. In general, anthropogenic and natural forcing plays a larger role in the global-scale climate change over periods longer than several decades, while internal climate variability can be more important within a few decades at local to continental scales [e.g., the Fifth Assessment Report (IPCC 2013); Hoerling et al. 2011; Xie et al. 2015; Sarojini et al. 2016].

The important role of internal climate variability on relatively small spatiotemporal scales has recently been highlighted in a number of studies. For example, Deser et al. (2012, 2014) analyzed North American climate projections over 2010–60 in two large ensembles of climate change simulations conducted with two climate models: the National Center for Atmospheric Research CCSM3 (40 simulations) and the Max Planck Institute ECHAM5 coupled model (17 simulations), respectively. Simulations within each ensemble are subject to the same external forcing but start from different conditions, thus

---

<sup>Ⓞ</sup> Supplemental information related to this paper is available at the Journals Online website: <https://doi.org/10.1175/JCLI-D-17-0366.s1>.

*Corresponding author:* Honghai Zhang, honghai.zhang@noaa.gov or honghaiz@princeton.edu

producing equally possible climate trajectories that consist of the same externally forced signal and different internally generated climate variability. Deser et al. (2012, 2014) found that both models project a substantial spread among ensemble members—caused solely by internal climate variability—in the 50-yr linear trends of surface temperature and precipitation, with trends of opposite signs for both fields appearing over many parts of North America. In particular, they showed that the spread in precipitation trends is larger than the forced signal, suggesting a dominant role of internal climate variability over anthropogenic forcing for precipitation. They further attributed the spread among ensemble members primarily to the low-frequency variations of large-scale atmosphere circulation. These studies, along with others (e.g., Wallace et al. 2015; Xie et al. 2015; Sarojini et al. 2016; Zhang et al. 2016), highlight the dominant role of internal climate variability in regional hydroclimate changes on decadal–multidecadal time scales.

The dominant role of internal climate variability in regional hydroclimate changes on decadal–multidecadal time scales suggests a challenge in detecting the associated anthropogenically forced component against the internal component. This is because internal climate variability is inherently unpredictable beyond a decade (e.g., Smith et al. 2007; Branstator et al. 2012; Yang et al. 2013). Previous studies (e.g., Deser et al. 2012, 2014) have implied that this challenge can be solved with large model ensembles. In this work, we use state-of-the-art large model ensembles to quantify the detectability of decadal hydroclimate changes caused by anthropogenic forcing in near-term projections over North America. We choose North America because the dominant role of internal climate variability in hydroclimate has been demonstrated there (Deser et al. 2012, 2014; Wallace et al. 2015). Many other studies have examined future projections of hydroclimate changes over North America based on simulations archived in phases 3 and 5 of the Coupled Model Intercomparison Project (CMIP) (e.g., Seager et al. 2007; Neelin et al. 2013; Maloney et al. 2014; Seager et al. 2014) and medium-sized single model ensembles (e.g., Lin et al. 2016; Sanderson et al. 2015; Lehner et al. 2017). These previous studies have focused on the future state of North American hydroclimate in response to projected anthropogenic forcing and the physical mechanisms underlying the anthropogenic changes. Here, we focus on the detectability of decadal-scale, anthropogenically forced hydroclimate changes against natural internal climate variability over North America in near-term projections.

This study is enabled by three state-of-the-art large ensembles of climate change experiments and three multimillennia preindustrial control experiments

conducted with two global climate models. The spatial resolution of the models (about  $0.5^\circ$  and  $1^\circ$ ; see more details below) allows the analysis to be conducted on regional scales (over North America). The large model ensemble has a special advantage in extracting the forced response by averaging across ensemble members that contain the same signal (forced response) but different noise (internal climate variability) and, thus, can facilitate the assessment of anthropogenic hydroclimate changes, especially on decadal time scales (dominated by internal climate variability). Here, we focus on the anthropogenic change in mean state (as opposed to the change in internal variability), which is the most predictable component in climate change (Kirtman et al. 2013). In particular, we examine the decadal evolution of projected changes in precipitation-minus-evaporation (PmE) mean state and assess when the changes become detectable and attributable to anthropogenic forcing against internal climate variability. Here, we characterize a change as “detectable” when the ensemble mean projected change in PmE between two time periods, such as the difference between the 2020–29 period and the 1950–99 period, lies outside the range of model simulated ensemble mean changes that arise solely from internal climate variability (as deduced from a corresponding control simulation). This study, focusing on North America, serves as an example to quantitatively illustrate that anthropogenically forced changes in hydroclimate mean state on regional and decadal scales are readily detectable. Our results are of relevance for local management of water resources, policy planning, and efforts in climate mitigation and adaptation over North America.

## 2. Models and experiments

The three large ensembles analyzed here are conducted with two state-of-the-art global coupled climate models: the Forecast-Oriented Low Ocean Resolution (FLOR) flux-adjusted model (Vecchi et al. 2014), developed at the Geophysical Fluid Dynamics Laboratory (GFDL), and the Community Earth System Model, version 1.0 (CESM1) (Hurrell et al. 2013), developed at the National Center for Atmospheric Research (NCAR) (see Table 1 for a summary). The GFDL FLOR has a high horizontal resolution of approximately 50 km for the atmosphere and land components and a relatively low horizontal resolution of  $1^\circ$  (telescoping to  $0.333^\circ$  near the equator) for the ocean and sea ice components, while the NCAR CESM1 has a nominal horizontal resolution of  $1^\circ$  for all model components (atmosphere, ocean, land, and sea ice). Note that the

TABLE 1. Summary of model simulations used in this study.

Expt	Description	Simulation	No. of model years analyzed
GFDL FLOR			
	~0.5° atmosphere and ~1° ocean		
Fully coupled control	Preindustrial forcing	3500 yr	3400 (101–3500)
30-member NATURAL	Natural historical forcing (solar variations and volcanos) before 2005; solar variability only (quasi-11-yr cycle) afterward.	1941–2050	3030 (1950–2050)
35-member ALLFORC	All historical forcing before 2005; RCP4.5 afterward.	5 members: 1861–2100 30 members: 1941–2050	3535 (1950–2050)
NCAR CESM1			
	~1° atmosphere and ocean		
Fully coupled control	Preindustrial forcing	2200 yr	1801 (400–2200)
Atmosphere–land control	Preindustrial forcing	2600 yr	2600
35-member ALLFORC	All historical forcing before 2005; RCP8.5 afterward.	1 member: 1850–2100 34 members: 1920–2100	5285 (1950–2100)

CCSM3 used by [Deser et al. \(2012, 2014\)](#) (at a horizontal resolution of approximately 2.8°) was the predecessor of the more advanced, higher-resolution CESM1.

Two of the three large ensembles are performed with FLOR. The first ensemble has 35 members, driven by identical observed estimates of both anthropogenic and natural forcing before 2005 and representative concentration pathway 4.5 (RCP4.5) emission scenario ([Meinshausen et al. 2011](#)) thereafter (termed ALLFORC), and the second ensemble has 30 members, driven by identical observed estimates of natural-only (volcanic and solar) forcing before 2005 and solar-only (no volcanic) forcing (quasi-11-yr cycle) thereafter (anthropogenic forcing fixed at the 1941 level) (termed NATURAL). Both ensembles simulate the period from 1941 to 2050, except for five ALLFORC members covering 1861–2100. Members within each ensemble start from different conditions that are briefly described as follows (refer to [Zhang et al. 2016](#) for more details). The five long members start from different years of a 3500-yr preindustrial control simulation (years 101, 141, 181, 221, and 261); the remaining 30 ALLFORC members and the 30 NATURAL members share the same initial conditions that are created by shuffling the 1940 and 1942 atmosphere–land states and 1941 ocean–sea ice states of the five long members. The first (second, third) 10 members start from the 1941 ocean–sea ice state of the first (second, third) long member, combined with the 1940 or 1942 atmosphere–land states of the five long members. We allow the model to adjust to the new initial conditions for the period 1941–50 and only analyze model output after 1950. The version of the FLOR model used here employs flux adjustments (FA), a technique for reducing mean biases in climate models. Companion versions of FLOR that do not use flux adjustments produce

similar changes in hydroclimate mean state in response to anthropogenic forcing ([Delworth et al. 2015](#)).

The CESM large ensemble analyzed here has 35 members ([Kay et al. 2015](#)). It simulates the period of 1921–2100, except for one member starting in 1850. All members are subject to identical observed estimates of historical (anthropogenic and natural) forcing before 2005 and RCP8.5 emission scenario ([Meinshausen et al. 2011](#)) thereafter, but they differ in their initial conditions (also termed ALLFORC; note its stronger RCP radiative forcing than FLOR ALLFORC). The long member (1850–2100) is initialized from year 402 of a 2300-yr preindustrial control simulation, while the remaining members branch off from the long member in year 1921, with round-off level differences added only to the air temperature field. Consistent with the FLOR ensembles, we only analyze model output after 1950.

Besides the three large ensembles of the climate change experiment, three preindustrial control simulations are also analyzed. These simulations include the aforementioned 3500-yr FLOR and 2300-yr CESM1 fully coupled control runs and a 2600-yr CESM1 control run only using its active atmosphere–land components driven by fixed boundary conditions (monthly mean sea surface temperature and sea ice averaged over years 402–1510 of the fully coupled control run). These long control simulations will be used to estimate low-frequency (decadal and longer) internal climate variability arising from the fully coupled system and the atmosphere–land intrinsic dynamics. This large volume of climate change and control simulations from the two climate models (a total of about 20 000 model years) provides a unique opportunity to robustly assess both forced climate change and internal climate variability, enabling us to investigate the detectability of decadal

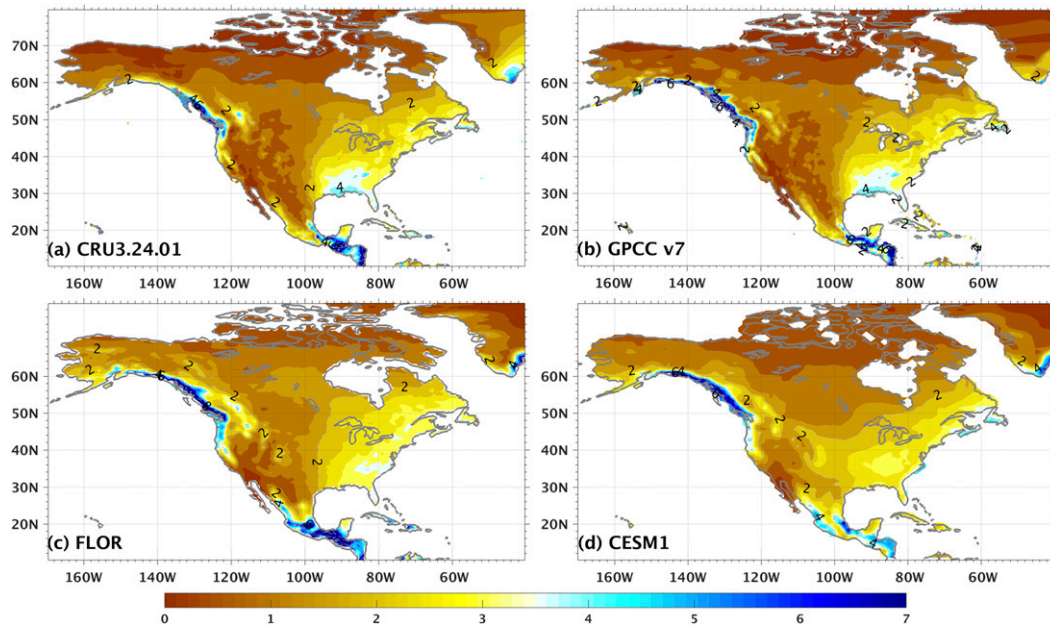


FIG. 1. Precipitation ( $\text{mm day}^{-1}$ ) climatology during 1950–99 in (a) CRU version 3.24.01, (b) GPCC version 7, (c) GFDL FLOR, and (d) NCAR CESM1. Model climatology is estimated as the average of the 35-member ALLFORC ensemble.

shifts in regional hydroclimate mean state caused by anthropogenic forcing in near-term projections. Here, we focus on the decadal evolution of PmE mean state over North America from 2000 to 2050.

The detectability analysis can be impacted by model biases and deficiencies. To evaluate the performance of the two climate models in simulating the hydroclimate over North America, we first compare the simulated climatological annual mean precipitation<sup>1</sup> during 1950–99 with observations (note that the lack of evaporation observations precludes a comprehensive evaluation of the model performance in hydroclimate). Two observational products are used: the Climatic Research Unit (CRU) at the University of East Anglia, version 3.24.01 (Harris et al. 2014), and the Global Precipitation Climatology Centre (GPCC) dataset, version 7 (Schneider et al. 2011),<sup>2</sup> both at  $0.5^\circ$  resolution. These two

observations exhibit consistent precipitation climatology over North America in terms of both spatial pattern and amplitude (except for Alaska and Greenland, where GPCC and CRU data show more precipitation, respectively; see Fig. 1). Both models capture the large-scale pattern of observed annual mean precipitation climatology, including enhanced precipitation along the northwestern Pacific coast, relatively strong precipitation over eastern North America, and weak precipitation over high latitudes and the  $120^\circ$ – $100^\circ$ W band. The higher-resolution FLOR, with the use of flux adjustments, simulates the east–west precipitation gradient much better than CESM1, but both models slightly overestimate the total precipitation over western North America and underestimate the precipitation over the southeastern United States. Overall, both models simulate a reasonable precipitation climatology during 1950–99 over North America [especially compared to their lower-resolution precedents, e.g., GFDL CM2.1 and NCAR CCSM3; refer to Delworth et al. (2015) and Zhang et al. (2016) for a detailed comparison].

To further evaluate the model performance, we also compare historical precipitation changes [(2000–15) minus (1950–99)] in observations with those simulated by the individual members of the ALLFORC ensembles (including components resulting from both external forcing and internal variability). The simulated precipitation changes are computed for each ALLFORC

<sup>1</sup> We have also evaluated the two models in terms of monthly mean precipitation variability (i.e., standard deviation) and found patterns of variability (Figs. S1 and S2 in the supplemental material) very similar to those of climatology (Fig. 1). The pattern similarity between climatology and variability is expected for monthly precipitation because it has a right-skewed probability distribution function bounded by zero (i.e., precipitation cannot be negative).

<sup>2</sup> The CRU data are available online at <https://doi.org/10.5285/D0E1585D-3417-485F-87AE-4FCECF10A992>, and the GPCC data are provided by the NOAA/OAR/ESRL Physical Sciences Division (Boulder, Colorado; <http://www.esrl.noaa.gov/psd/>).

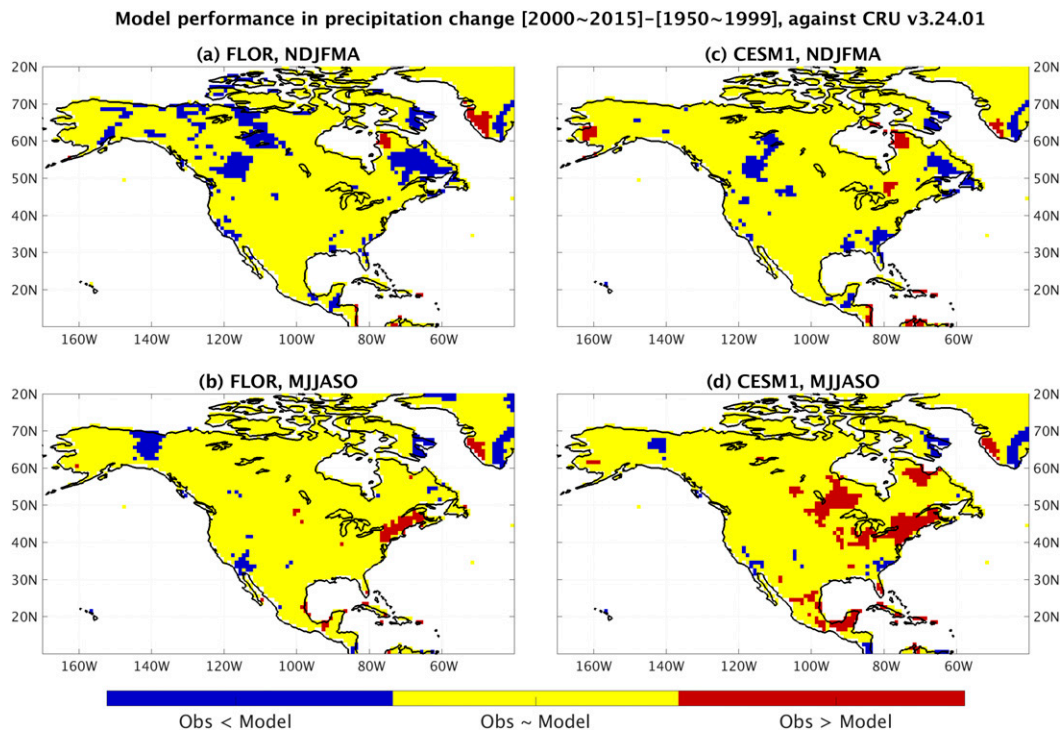


FIG. 2. Model performance in historical changes of land precipitation between 2000–15 and 1950–99 against the CRU observations. (a),(b) FLOR and (c),(d) CESM1 for (top) NDJFMA and (bottom) MJJASO, respectively. Yellow color denotes that models are consistent with observations, which is defined when observed changes are within the distribution of those simulated by the ALLFORC ensemble. Blue (red) color indicates that observed changes are smaller (larger) than all simulated changes from the 35 ALLFORC members.

ensemble member; the range of the 35-member changes is then compared with observations. Models are considered to be consistent with observations when the observed historical precipitation changes are within the range of modeled changes. Figure 2 shows that models are consistent with observations (indicated by yellow color) over most of North America (similar results with GPCP data, not shown). The inconsistency over a few scattered regions (blue and red color) is not systematic across seasons (i.e., does not appear in both seasons in the same model) and can arise from a number of reasons: 1) poor model performance, 2) not large enough ensemble size, and 3) observational errors. Overall, both models simulate historical changes in precipitation that are consistent with observations over most of North America. This consistency further increases our confidence in the utility of the models in investigating the detectability of anthropogenic changes in hydroclimate mean state in future projections.

### 3. Methods

Using the three large ensembles, we are able to assess the near-term projections of decadal shifts in PmE mean

state over North America caused by external (anthropogenic and natural) forcing. Within each ensemble, PmE mean state is defined for each decade between 2000 and 2050 as the ensemble average (for the 35-member ALLFORC, this translates to 350 simulated years that are used to calculate the decadal mean; for the 30-member NATURAL ensemble, it is 300 simulated years). These consecutive decadal mean states, describing the decadal evolution of PmE during 2000–50, are then compared with the past 50-yr climatology averaged over 1950–99 (1750 and 1500 model years for the 35-member ALLFORC and 30-member NATURAL ensembles, respectively) to highlight the shifts in PmE mean state.

To test if the shifts are caused by external forcing or random low-frequency internal climate variability, we make use of the preindustrial control simulations with a Monte Carlo approach. For each control simulation, we do the following: at each grid point, we first randomly select a 10-yr period (to mimic any decade in the period 2000–50) and a second, nonoverlapping 50-yr period (to mimic 1950–99) and then compute the difference between the time mean of the 10-yr period and the time mean of the 50-yr period—this difference results only

from internal climate variability. We repeat this  $N$  times (the value of  $N$  is described below) to form the grand ensemble of these differences and compute the ensemble average. We then repeat the above process 5000 times to create a distribution of such ensemble mean differences that could occur simply by chance from internal climate variability. We use  $N = 30$  when evaluating the projected changes in the 30-member NATURAL ensemble and  $N = 35$  when evaluating the projected changes in the 35-member ALLFOR ensembles. The range of the distribution is used to assess the detectability of shifts in PmE mean state in future projections: shifts “outside the range” are attributable to external forcing and defined as detectable.

The Monte Carlo method is carried out at each grid point and can be applied to any regions. A caveat of this Monte Carlo method is that it is based on the assumption that internal climate variability remains stationary from preindustrial control simulations to future projections. We have compared PmE low-frequency internal variability between the control simulations and the large ensembles and found that changes in PmE internal variability in the future are relatively small, and our results are not sensitive to account for these changes (see [appendix A](#)). Future shifts in PmE mean state over North America are assessed for cold [November–April (NDJFMA)] and warm [May–October (MJJASO)] seasons separately.

## 4. Results

### *a. Decadal evolution of PmE mean state during 2000–50*

Despite the differences between FLOR and CESM1 (e.g., model resolution and configuration), the projected PmE mean state (ensemble average) over North America exhibits similar systematic changes during 2000–50 (relative to the 1950–99 reference period) in the two ALLFORC ensembles ([Figs. 3 and 4](#)). The projected PmE mean state, in general, shifts toward wetter conditions over high latitudes and drier conditions over subtropical to middle latitudes, which is consistent with previous findings based on the CMIP5 multimodel ensemble (e.g., [Seager et al. 2014](#); [Maloney et al. 2014](#)) and has been largely explained by the “wet get wetter, dry get drier” mechanism ([Held and Soden 2006](#)). These projected PmE changes, however, are not all distinguishable from low-frequency internal climate variability in each decade and, thus, cannot be unambiguously attributed to external forcing.

In boreal winter (NDJFMA; [Fig. 3](#)), moistening trends in PmE mean state are projected over most North

American land regions, except southwestern North America, with a drying trend in both models; over the ocean, there is a general subpolar moistening north of about 40°N and subtropical drying to the south. During the decade of 2000–09 in both models, a small portion of the subtropics—mostly ocean—shows drying changes that are beyond the range of internal climate variability and remain detectable thereafter. As expected, the area of detectable changes in PmE mean state increases accordingly with external forcing, including the anthropogenic component, and mainly over high latitudes and subtropics; in contrast, the FLOR NATURAL ensemble projects PmE changes that are mostly inside the range of internal climate variability, suggesting a crucial role for anthropogenic forcing in projected future changes in PmE mean state during winter. Over land, a notable region is northeastern North America near the Great Lakes (40°–55°N, 60°–85°W; blue box in [Fig. 3](#)), where both models project early (around the 2010s) detectable moistening of comparable magnitudes; another notable region is southwestern North America (20°–40°N, 100°–120°W; blue box in [Fig. 3](#)), where the drying trend appears detectable in FLOR starting around the 2000s but much later in CESM1 (around the 2050s, despite its stronger RCP8.5 forcing; shown later in [Fig. 10](#)).

The bottom row of [Fig. 3](#) shows the timing of detectable PmE changes—defined as the decade when the ensemble mean PmE changes first become detectable (against internal variability from control simulations) and remain so thereafter (relative to the 1950–99 reference period). Note that for FLOR, the PmE changes that first become detectable during the 2040s are not necessarily detectable because no information thereafter is available, but this case only accounts for a small fraction of North America (2%–8%) ([Fig. 5 and Table A1](#)). In both models, early detectability of PmE changes caused by anthropogenic forcing is projected over high latitudes and subtropics around the 2000s and 2010s, while the PmE changes in middle latitudes around 40°N remain indistinguishable from internal climate variability throughout 2000–50. In general, FLOR projects earlier detectability of anthropogenic signal than CESM1, which will be discussed in the next section.

In boreal summer (MJJASO; [Fig. 4](#)), the spatial pattern of northern moistening and southern drying is similar to that in winter but shifts northward, with the subtropical drying expanding into middle latitudes during 2000–50. In both models, a weak drying trend is projected over most of central North America, and a moistening trend is projected over northwestern North America (Alaska and nearby area); however, the northwestern moistening appears detectable only in

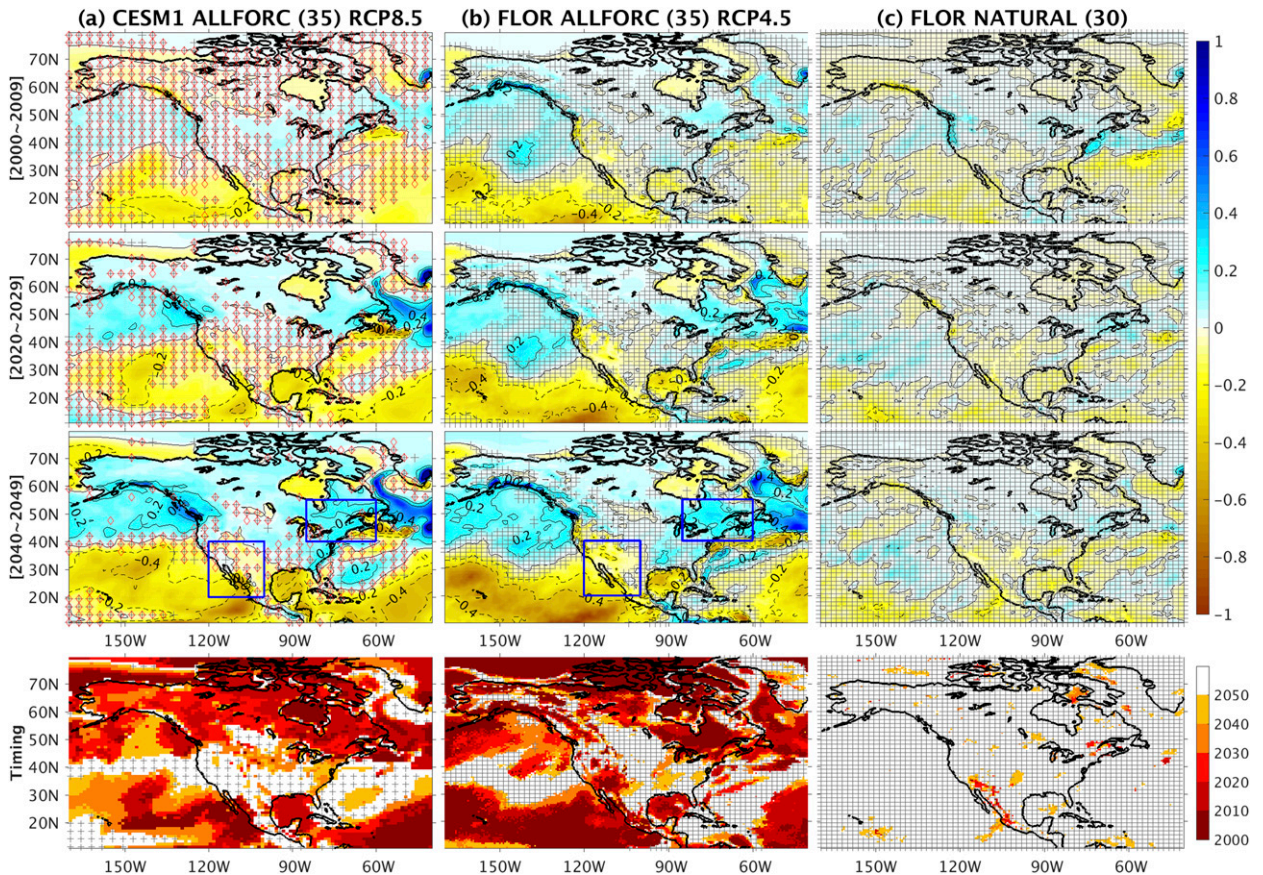


FIG. 3. Decadal evolution of changes in wintertime (NDJFMA) PmE mean state (shading) relative to the 1950–99 climate during the (top) 2000s, (middle top) 2020s, and (middle bottom) 2040s (decades as denoted to the left of the figure; note that the 2010s and 2030s are not shown to allow more space and enhanced clarity for the periods shown) in (a) CESM1 ALLFORC RCP8.5, (b) FLOR ALLFORC RCP4.5, and (c) FLOR NATURAL. Contours with interval  $\pm 0.2 \text{ mm day}^{-1}$  are labeled in black, with dashed contours denoting negative PmE changes. Gray crosses in all three columns denote that changes in PmE mean state are not detectable against internal climate variability estimated from fully coupled control simulations (see section 3 for details on the detectability analysis); red diamonds in (a) denote undetectable against internal climate variability estimated from the atmosphere–land-only control simulation of CESM1. (bottom) Timing of detectable changes in PmE mean state, defined as the first decade when PmE changes become detectable and remain detectable thereafter. Gray crosses in the bottom row mean no detectability by 2050 and are the same as those crosses for the 2040s (i.e., the row above). [Blue boxes in the row for the 2040s in (a),(b) indicate the land regions used for the average in Figs. 7 and 8.]

CESM1, while the drying over central North America is detectable starting around the 2000s in both models. Note that the FLOR NATURAL ensemble projects a weak drying over central North America that has a similar spatial pattern to the ALLFORC ensemble; this similarity can be explained by the fact that the NATURAL ensemble includes volcanic cooling only before 2005, and, thus, future changes relative to 1950–99 are qualitatively equivalent to those in a future warming scenario. Furthermore, projected drying changes in NATURAL appear detectable over eastern- and western-central North America, where detectable PmE changes are projected in ALLFORC. The early detectability in both ALLFORC and NATURAL over these regions is due to the weak internal PmE variability during MJJASO (Fig. 6; see more

discussion in the next section). The projected detectable drying over eastern- and western-central North America can be attributed to natural forcing in NATURAL but cannot be attributed exclusively to anthropogenic forcing in ALLFORC because the same natural forcing is also included. Note that this does not mean anthropogenic forcing is not important; in fact, subtracting NATURAL from ALLFORC—an estimate of the contribution from anthropogenic forcing—only slightly weakens the detectability projected in ALLFORC (not shown), which corroborates the role for anthropogenic forcing.

The timing of detectable PmE changes during MJJASO is shown in the bottom row of Fig. 4. Early detectability of projected PmE changes is simulated in central North America in both models, although the specific regions are

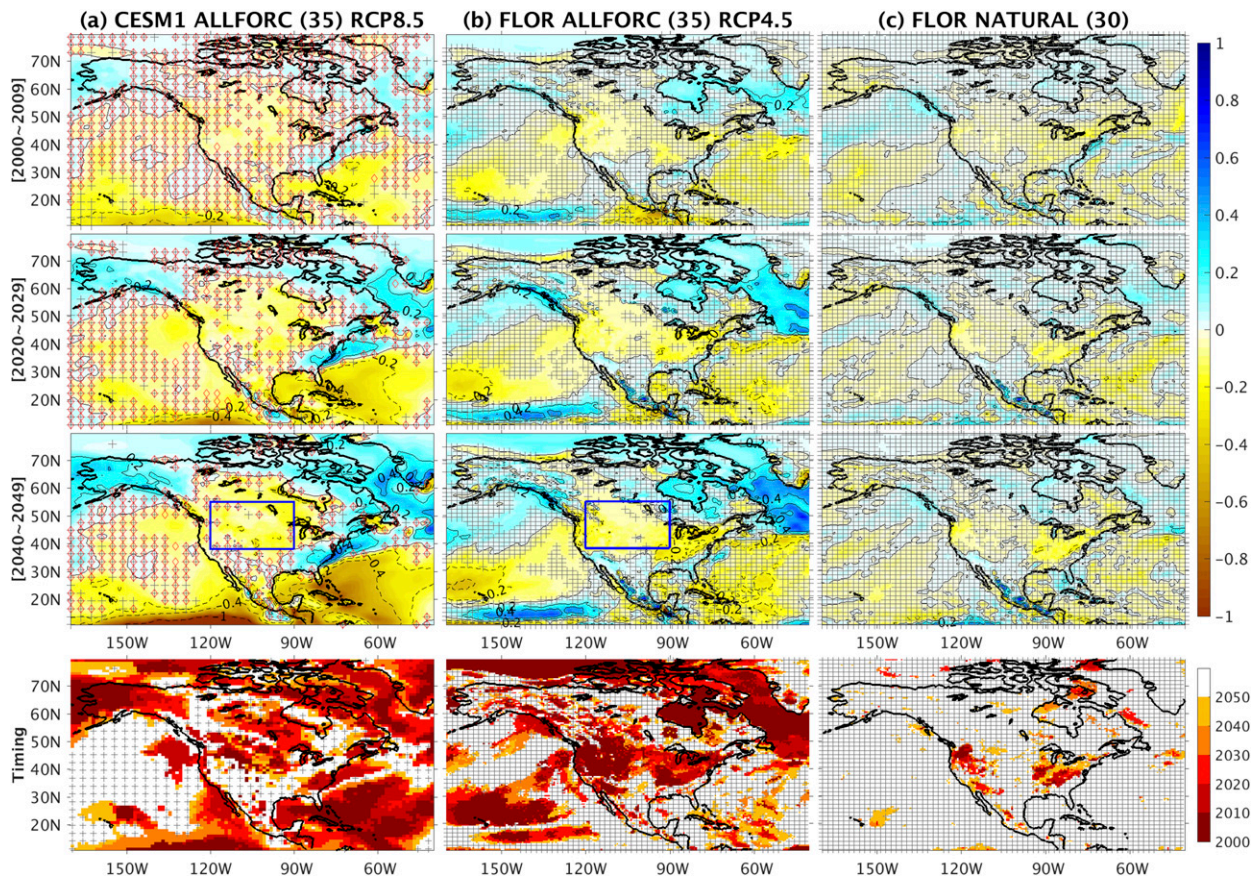


FIG. 4. As in Fig. 3, but for MJJASO. [Blue boxes in the row for the 2040s in (a),(b) indicate the region used for the average in Fig. 9.]

slightly different, with the earliest detectability in western-central North America ( $35^{\circ}$ – $50^{\circ}$ N,  $100^{\circ}$ – $120^{\circ}$ W) in FLOR and in mid-central North America ( $40^{\circ}$ – $60^{\circ}$ N,  $80^{\circ}$ – $110^{\circ}$ W) in CESM1. In addition, early detectability is also projected over high latitudes in both models. Similar to the wintertime projections, the timing of detectable PmE changes during MJJASO is earlier in FLOR than in CESM1 over most of North America.

To quantify the decadal evolution of detectable changes in PmE mean state over North America, we show the fraction of the area with detectable PmE changes as a function of time in Fig. 5 (cyan, blue, and red bars). As expected, the fraction of the area with detectable PmE changes in both models increases with time; the rate of increase is much larger in ALLFORC than in NATURAL for FLOR, suggesting a crucial role of anthropogenic forcing in the shifts of PmE mean state. The increase in the fraction of the total area over North America has comparable contributions from land and ocean in both seasons. During winter, the fraction of the total area with detectable PmE changes increases from about 33% (19%) in the 2000s to about 70% (72%) in the 2040s in FLOR (CESM1), while during summer, it

increases from 27% (21%) in the 2000s to about 54% (64%) in the 2040s in FLOR (CESM1). The rate of increase is, therefore, larger in CESM1, consistent with its stronger RCP8.5 emission scenario. The detectable changes in PmE mean state can largely be attributed to anthropogenic forcing, particularly during winter. During summer, the FLOR NATURAL ensemble projects a fairly large fraction of land area with detectable PmE changes, about 20% by the 2040s, that can also be attributed to natural forcing (volcanic cooling before 2005 and no volcanic forcing thereafter); over these regions, a clean attribution between natural and anthropogenic forcing requires another large ensemble similar to NATURAL but driven only by anthropogenic forcing, which, however, is not available. Nonetheless, the large differences between ALLFORC and NATURAL during both seasons highlight the crucial role of anthropogenic forcing in the detectable shifts of PmE mean state over North America.

#### b. Mechanisms

Why do projected changes in PmE mean state have different timing of detectability against internal

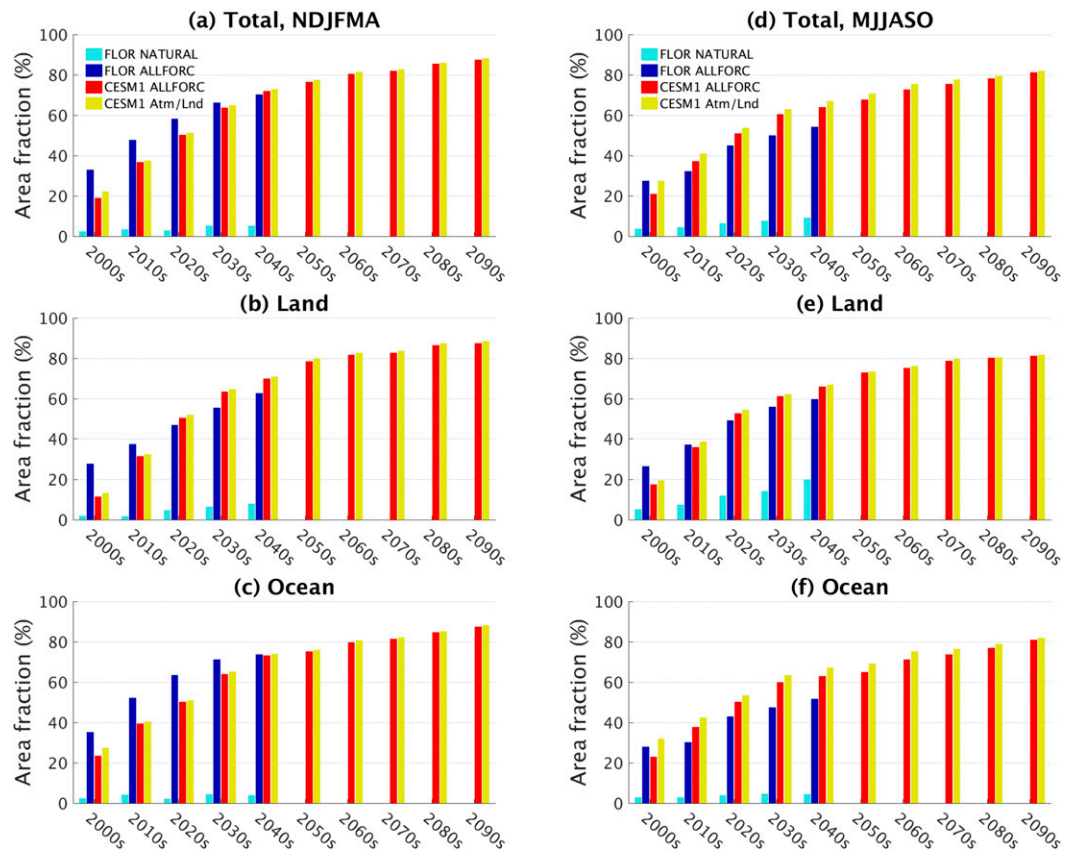


FIG. 5. Fraction of area with detectable changes in PmE mean state in (a)–(c) winter and (d)–(f) summer over North America ( $10^{\circ}$ – $80^{\circ}$ N,  $40^{\circ}$ – $170^{\circ}$ W) for (top) total area, (middle) land, and (bottom) ocean. Cyan, blue, and red bars show fraction of area with detectable changes against fully coupled internal climate variability in FLOR NATURAL, ALLFORC, and CESM1 ALLFORC, respectively, while yellow bars denote that in CESM1 ALLFORC against atmosphere–land internal climate variability.

climate variability over different regions of North America? To answer this question, we present in Fig. 6 the range of low-frequency internal climate variability from fully coupled control simulations used in the detectability analysis. Low-frequency internal variability exhibits a similar spatial pattern between the two models (during the same season). It is relatively weak over high latitudes and the western half of North America (about  $120^{\circ}$ – $100^{\circ}$ W) and relatively strong over the northwestern Pacific coast and eastern North America along the coast, a pattern that is consistent with the mean PmE structure (not shown; as expected, considering the fact that precipitation cannot be negative, and evaporation is also largely one direction from Earth’s surface to atmosphere) (e.g., He et al. 2017).

The different timing of detectable shifts in PmE mean state can be explained by comparing projected PmE changes to the range of low-frequency internal climate variability (i.e., signal-to-noise ratio). Over

high latitudes, where projected PmE changes are weak (below  $0.1 \text{ mm day}^{-1}$  moistening), the early detectability of shifts in PmE mean state arises from the weak, low-frequency internal climate variability (so that even small changes can easily go beyond the range of internal climate variability); over the subtropics (mostly ocean), where low-frequency internal climate variability is relatively strong, the early detectability of shifts in PmE mean state is due to the large magnitude of projected PmE changes (above  $0.2 \text{ mm day}^{-1}$  drying). In winter, northeastern North America (northeast of the Great Lakes) has early detectability of moistening in PmE mean state in both models, mainly because of the strong projected PmE changes; southwestern North America ( $20^{\circ}$ – $40^{\circ}$ N,  $100^{\circ}$ – $120^{\circ}$ W) exhibits earlier detectability of drying in PmE mean state in FLOR than in CESM1 because FLOR simulates slightly weaker internal variability but projects stronger drying, compared to CESM1. In summer, the early detectability of drying over central

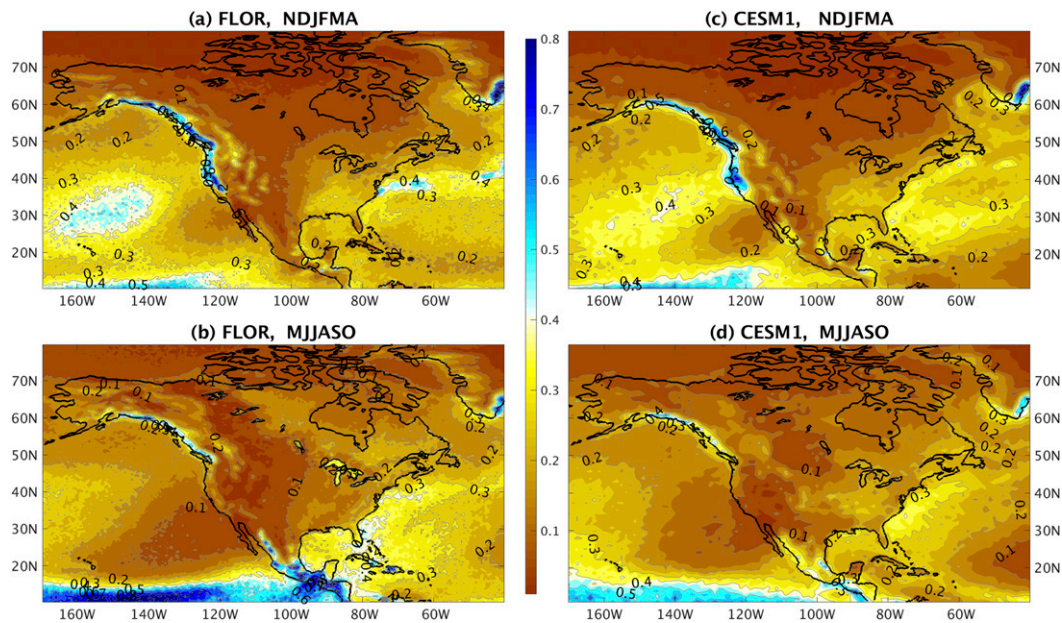


FIG. 6. Range of internal PmE variability ( $\text{mm day}^{-1}$ ) in fully coupled control simulations used in the detectability analysis in Figs. 3 and 4 in (a),(b) FLOR and (c),(d) CESM1 during (top) NDJFMA and (bottom) MJJASO. The range is estimated as the difference between the maximum and minimum values of the 5000 samples constructed with the Monte Carlo approach (see text for more details).

North America in both models is attributed to the weak, low-frequency internal climate variability because the projected drying is weak (in all three ensembles).

In CESM1, PmE low-frequency internal climate variability is also examined in the atmosphere–land-only control simulation and is found to be similar to that in the fully coupled simulation (not shown). As a result, the decadal evolution of detectable PmE changes is nearly the same between using internal climate variability in fully coupled and atmosphere–land-only control simulations in both seasons (Figs. 3a and 4a, gray vs red hatching; Fig. 5, red and yellow bars). This similarity suggests that the PmE low-frequency internal climate variability over North America is dominated by atmosphere–land intrinsic dynamics, consistent with the findings on precipitation by Deser et al. (2014).

Differences in the timing of detectability between the two models are not so surprising, considering their different amplitudes of internal climate variability and projected PmE changes (arising presumably from different model configuration, such as resolution, forcing, and model physics), but what is interesting here is their similarities over a few key regions, including northeastern ( $40^{\circ}$ – $55^{\circ}$ N,  $60^{\circ}$ – $85^{\circ}$ W), southwestern ( $20^{\circ}$ – $40^{\circ}$ N,  $100^{\circ}$ – $120^{\circ}$ W), and central ( $38^{\circ}$ – $55^{\circ}$ N,  $90^{\circ}$ – $120^{\circ}$ W) North America. We next show that the physical processes underlying the shifts in PmE mean state in these regions are also similar between the two models.

To isolate contributions of various processes to the PmE changes, we perform moisture budget analysis (e.g., Seager and Henderson 2013). The atmosphere moisture equation can be expressed in vertically integrated form on the pressure coordinate as

$$P - E = -\frac{1}{\rho_w g} \frac{\partial}{\partial t} \int_0^{p_s} q \, dp - \frac{1}{\rho_w g} \nabla \cdot \int_0^{p_s} \mathbf{u} q \, dp, \quad (1)$$

where, on the left-hand side,  $P$  and  $E$  are precipitation and evaporation, respectively, and on the right-hand side,  $\rho_w$ ,  $g$ ,  $p_s$ ,  $q$ , and  $\mathbf{u}$  are water density, gravitational acceleration, surface pressure, atmospheric specific humidity, and winds, respectively. The equation states that the net water flux at the surface (i.e., PmE) is balanced by the tendency in total (vertically integrated) atmospheric moisture content (first term on the right-hand side) and the divergence of total atmospheric moisture flux (second term on the right-hand side). To diagnose specific processes, such as moisture advection and atmospheric flow divergence, the divergence term needs to be decomposed into

$$-\frac{1}{\rho_w g} \nabla \cdot \int_0^{p_s} \mathbf{u} q \, dp = -\frac{1}{\rho_w g} \int_0^{p_s} \nabla \cdot (\mathbf{u} q) \, dp - \frac{1}{\rho_w g} q_s \mathbf{u}_s \cdot \nabla p_s, \quad (2)$$

where the first term on the right-hand side—vertical integral of moisture flux divergence—can be further decomposed into

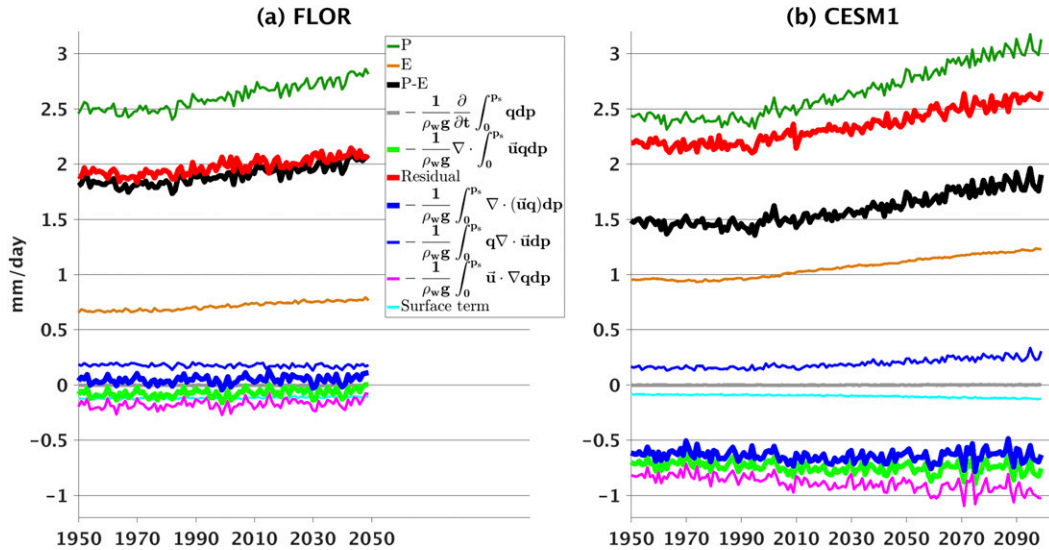


FIG. 7. The 35-member ensemble mean moisture budget in (a) FLOR and (b) CESM1 during winter (NDJFMA), averaged over northeastern North America ( $40^{\circ}$ – $55^{\circ}$ N,  $60^{\circ}$ – $85^{\circ}$ W, land only; refer to the blue box in Figs. 3a,b for the 2040s). Moisture budget analysis is based on monthly mean fields, and moisture budget terms are indicated in the legend. Note that variations of the residual term (red curve) can be largely interpreted as contributions from unresolved submonthly transient eddies (see appendix B); here, the 35-member ensemble mean removes part of internal climate variability and should be interpreted as the diagnostics of hydroclimate mean state. FLOR covers 1950–2050 and CESM1 1950–2100.

$$-\frac{1}{\rho_w g} \int_0^{p_s} q \nabla \cdot \mathbf{u} dp - \frac{1}{\rho_w g} \int_0^{p_s} \mathbf{u} \cdot \nabla q dp,$$

a term related to flow divergence and a term related to moisture advection. The second term on the right-hand side represents the contribution from vertical moisture flux at the surface (indicated by the subscript  $s$ ) owing to the flow along the sloping topography and in models is computed as a residual of Eq. (2) (i.e., the difference between the divergence of total moisture flux and the vertical integral of moisture flux divergence).

Here, in the three large ensembles,  $p_s$ ,  $q$ , and  $\mathbf{u}$  are saved at the monthly mean resolution for the entire simulation period. Using monthly mean fields, the moisture budget will have a residual—the imbalance between the left- and right-hand sides of the moisture Eq. (1)—that includes numerical errors (from discretization) and unresolved submonthly processes (i.e., transient eddies). To quantify contributions from submonthly transient eddies in the moisture budget analysis, high-frequency (at least 6 hourly) model output are required (Seager and Henderson 2013). However, we find that variations of the monthly mean residual are dominated by submonthly transient eddies (see appendix B for analyses supporting this assertion). Therefore, trends (of interest here) in the monthly mean residual can be interpreted as the contribution from unresolved, submonthly transient eddies.

Over northeastern North America ( $40^{\circ}$ – $55^{\circ}$ N,  $60^{\circ}$ – $85^{\circ}$ W) in both models, the wintertime moistening trend in PmE (black curve in Fig. 7) results from a larger rate of increase in precipitation (thin dark green curve) than in evaporation (thin brown curve). Among various processes in the moisture budget, only the residual term (red curve) shows a similar trend to PmE, suggesting that the wintertime moistening in this region is caused by submonthly transient eddies. The role of wintertime submonthly transient eddies in moistening the northeast is likely attributable to the poleward shift and enhancement of storm tracks (e.g., Yin 2005; Bengtsson et al. 2006; Wu et al. 2011) and/or the strengthened meridional gradient of atmospheric moisture content (Seager et al. 2014)—both as a result of greenhouse gas-induced global warming. The poleward shift and enhancement of storm tracks can lead to moistening via stronger transient eddy activity over northeastern North America, while the strengthened meridional atmospheric moisture gradient does not require changes in transient eddy activity for the northeastern moistening and is shown to be the dominant process in the CMIP5 ensemble (Seager et al. 2014).

Over southwestern North America ( $20^{\circ}$ – $40^{\circ}$ N,  $100^{\circ}$ – $120^{\circ}$ W) during winter, FLOR and CESM1 simulate contrasting wet and dry PmE mean states, respectively (owing to the different relative amplitudes of precipitation and evaporation mean state; Fig. 8). However,

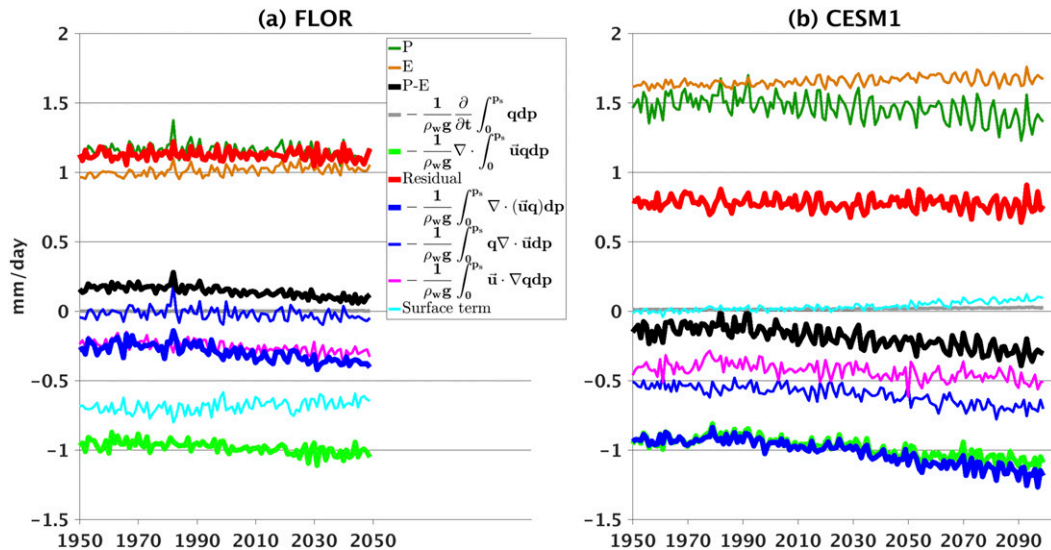


FIG. 8. As in Fig. 7, but for southwestern North America ( $20^{\circ}$ – $40^{\circ}$ N,  $100^{\circ}$ – $120^{\circ}$ W, land only; refer to the blue box in Figs. 3a,b for the 2040s) during NDJFMA.

both models project a positive trend in evaporation, a relatively weak negative trend in precipitation, and, thus, the drying trend in PmE. In contrast to northeastern North America, submonthly transient eddies (indicated by the residual term; red curve) in both models show no detectable trend; instead, the drying PmE trend is attributed to an increase in the divergence of total moisture flux by monthly mean atmospheric circulation (thick light green curve). The increase in the divergence of total moisture flux has a positive contribution from the vertical integral of moisture flux divergence (blue curve) that is partly offset by the surface term (cyan curve) in both models; however, the increase in the vertical integral of moisture flux divergence is explained in FLOR only by the moisture advection term (magenta curve) and in CESM1 by both the moisture advection and atmospheric flow divergence (thin light blue curve) terms. Despite these differences, FLOR and CESM1 both simulate a dominant role of moisture flux divergence by monthly mean circulation (as opposed to submonthly transient eddies) in the projected wintertime drying trend in PmE mean state over southwestern North America, a result that is consistent with previous findings on the moisture budget in this region (e.g., Seager et al. 2007, 2014).

The moisture budget is also examined over central North America ( $38^{\circ}$ – $55^{\circ}$ N,  $90^{\circ}$ – $120^{\circ}$ W), where both models project detectable PmE drying during summer (Fig. 9). The drying trend arises primarily from the enhanced evaporation and is largely consistent with the negative trend of monthly residual term dominated by submonthly transient eddies in both models (Fig. B2),

suggesting an important role of submonthly transient eddies in the projected summertime drying there. FLOR and CESM1 disagree in the trends of monthly mean moisture processes. FLOR projects a weak negative trend (or no trend) in the divergence of total moisture flux (thick green curve), while CESM1 projects a positive trend that partly offsets the contribution from submonthly transient eddies; the breakdown terms from the divergence of total moisture flux, in general, show opposite trends between FLOR and CESM1 (e.g., blue curves). Despite these differences in monthly mean processes, the suggested role of submonthly transient eddies in projected summertime drying here aligns with the conclusion by Seager et al. (2014), who used CMIP5 6-hourly output to explicitly show a similar role of submonthly transient eddies in this region.

### c. Decadal evolution of PmE mean state during 2050–2100 in CESM1

In the CESM1 large ensemble, we extend the above analysis and assess the decadal evolution of PmE mean state during 2050–2100. As shown in Fig. 10, the spatial pattern of PmE changes in both seasons remains largely the same as that during the 2040s, but the magnitude keeps growing in response to the RCP8.5 radiative forcing. As a result, the area of detectable PmE changes in winter (summer) increases from about 72% (64%) of North America during the 2040s to about 87% (81%) during the 2090s (Fig. 5). Regions of undetectable PmE changes are mainly confined to the transition zone between moistening and drying (where the changes are nearly zero). Note that these results on the detectability

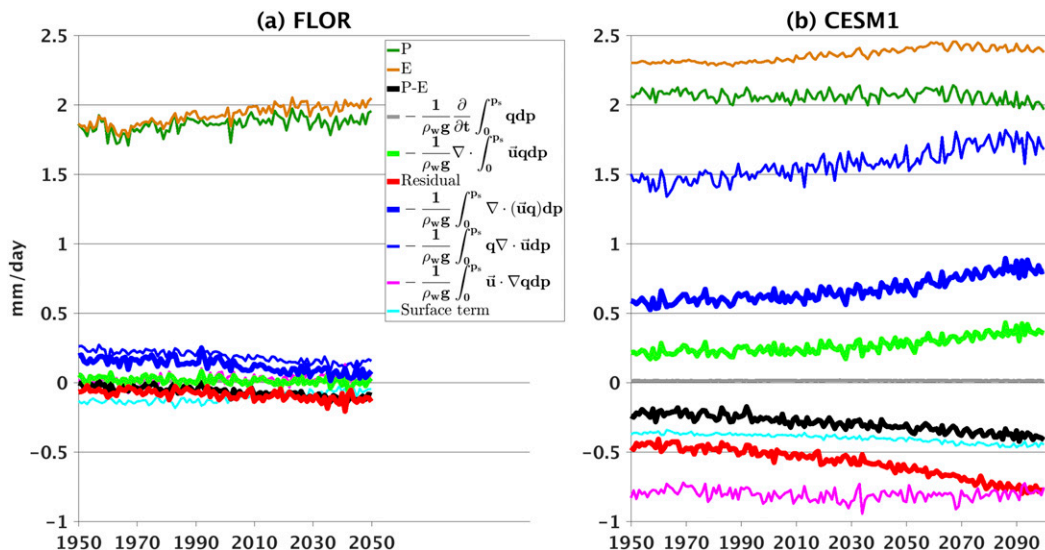


FIG. 9. As in Fig. 7, but for central North America ( $38^{\circ}$ – $55^{\circ}$ N,  $90^{\circ}$ – $120^{\circ}$ W; refer to the blue box in Figs. 4a,b for the 2040s) during MJJASO. Note that precipitation and evaporation curves have been shifted downward by  $1 \text{ mm day}^{-1}$  in both models in order to make the plot smaller.

remain largely the same when the atmosphere–land-only control simulation is used (Figs. 10 and 5).

The timing of detectable PmE changes for the entire twenty-first century is shown in the bottom row of Fig. 10. The spatial pattern of the timing is largely similar to that for the 2000–50 period (Figs. 3 and 4, bottom row) because more than 60% of North America already exhibit detectable PmE changes before 2050, while only about 15% of North America first become detectable during 2050–2100 (Fig. 5). Note that the smaller rate of increase in area with detectable signal during 2050–2100 does not imply that impacts from anthropogenic forcing get weaker; instead, the magnitude of projected PmE changes—with a spatial pattern stabilized by 2050—keeps increasing, along with the growing anthropogenic radiative forcing (Fig. 10), suggesting enhanced impacts of anthropogenic forcing during the second half of the twenty-first century.

## 5. Summary and discussion

In this work, we have assessed the detectability of decadal changes in hydroclimate mean state caused by anthropogenic forcing in future projections over North America. We use three large ensembles with projected radiative forcing changes—two with the GFDL FLOR model and one with the NCAR CESM1—along with three multimillennia preindustrial control simulations (one with FLOR and two with CESM1). This large volume of simulations (a total of about 20 000 model years) and the high spatial resolution ( $\sim 50 \text{ km}$ ) of FLOR

atmosphere–land components enable a robust assessment of anthropogenic changes in hydroclimate mean state on the regional scale and decadal time scales. Here, we have focused on the detectability of anthropogenic shifts in precipitation-minus-evaporation mean state over North America during 2000–50 relative to the 1950–99 climate for cold (NDJFMA) and warm (MJJASO) seasons, respectively. Both FLOR and CESM1 simulate reasonable precipitation climatology during 1950–99, compared to observations over North America. In addition, they also simulate historical precipitation changes consistent with observations over most of North American land.

Despite many model differences (e.g., resolution and external forcing), the FLOR and CESM1 ALLFORC ensembles project similar robust features in the decadal evolution of PmE mean state over North America during 2000–50. Relative to the 1950–99 climate, PmE mean state is projected to get wetter (i.e., more positive) in high latitudes and drier in subtropics, a pattern of changes that is consistent with previous studies (e.g., Hoerling et al. 2011; Seager et al. 2014; Maloney et al. 2014) and has been explained by the “wet get wetter, dry get drier” mechanism (Held and Soden 2006) in response to anthropogenic global warming. These projected changes in PmE mean state, however, are not all detectable against internal climate variability estimated from preindustrial control simulations and, thus, not all attributable to anthropogenic forcing. During the 2000s, detectable changes in PmE mean state only appear in a few regions of the high latitudes and subtropical ocean

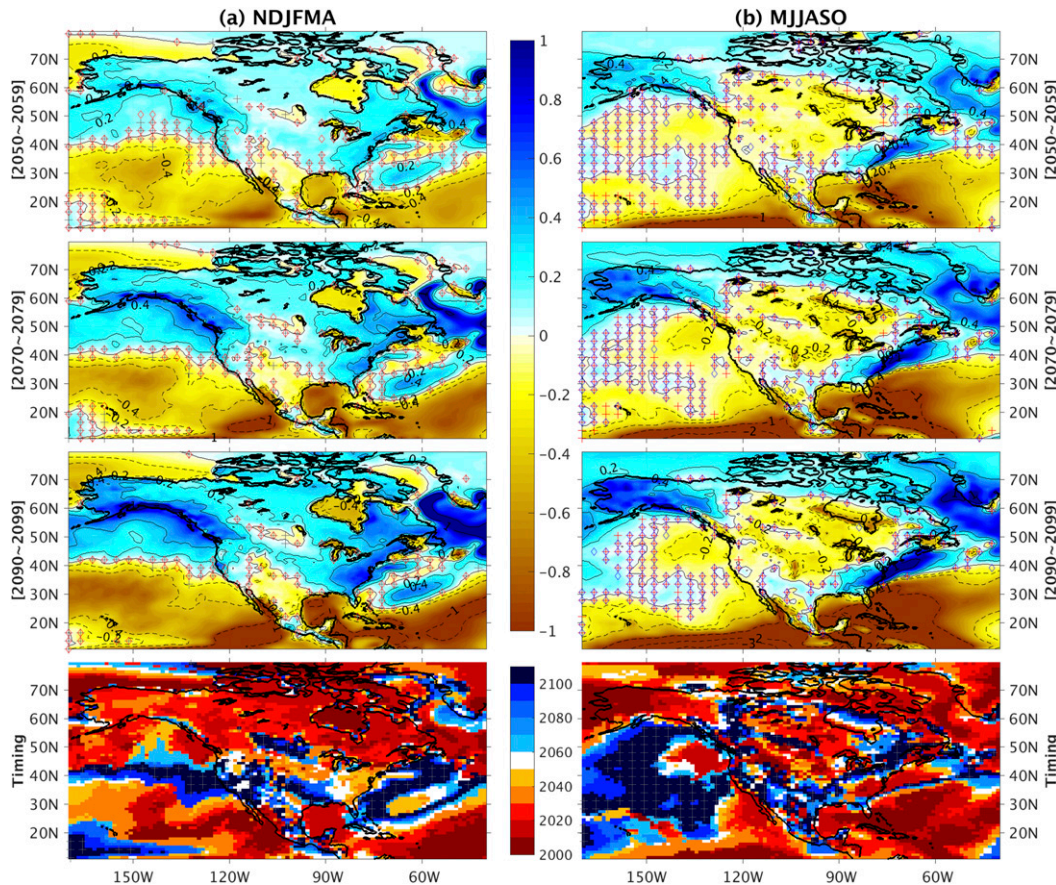


FIG. 10. As in Fig. 3a and 4a, but for projections during 2050–2100 in the CESM1 ensemble in (a) NDJFMA and (b) MJJASO, respectively. Note that the 2060s and 2080s are not shown for clarity.

in NDJFMA and in central North America in MJJASO; as radiative forcing increases, the changes expand to a larger area (expected) and cover about 50%–70% of North America by the 2040s. The time of emergence of detectable changes in PmE mean state against internal climate variability depends on the signal-to-noise ratio. Over high latitudes and summertime central North America, the early emergence of detectable changes in PmE mean state is due to the weak internal climate variability in PmE, while in the subtropics, it is mainly due to the large projected PmE changes. In regions without detectable changes in PmE mean state, the lack of detectability by the 2040s is because of a combination of relatively strong internal climate variability and relatively weak projected PmE changes.

The FLOR NATURAL ensemble can help further attribute detectable changes in PmE mean state into anthropogenic and natural forcing. In NDJFMA, projected PmE changes in NATURAL remain indistinguishable from internal climate variability throughout 2000–50 over most of North America, which suggests that detectable changes in PmE mean state projected in ALLFORC are

attributable to anthropogenic forcing. In MJJASO, detectable drying in PmE mean state is projected in both NATURAL and ALLFORC over parts of central North America, owing to the weak PmE internal variability. While the detectable PmE changes projected in NATURAL in these regions can be attributed to natural forcing (volcanic cooling before 2005 but no volcanic forcing whatsoever thereafter), those in ALLFORC (in the same regions) are not exclusively attributable to anthropogenic forcing because the same natural forcing is included (note that this does not mean that anthropogenic forcing is not important, but only means that an exclusive attribution cannot be achieved with the two ensembles here; a clean exclusive attribution requires an additional large ensemble driven only by anthropogenic forcing). The weak PmE internal climate variability over central North America implies that the hydroclimate mean state is vulnerable to external forcing during MJJASO.

Over North American land, there are a few notable regions where projected changes in PmE mean state are similar in both models, including northeastern and southwestern North America in NDJFMA and central

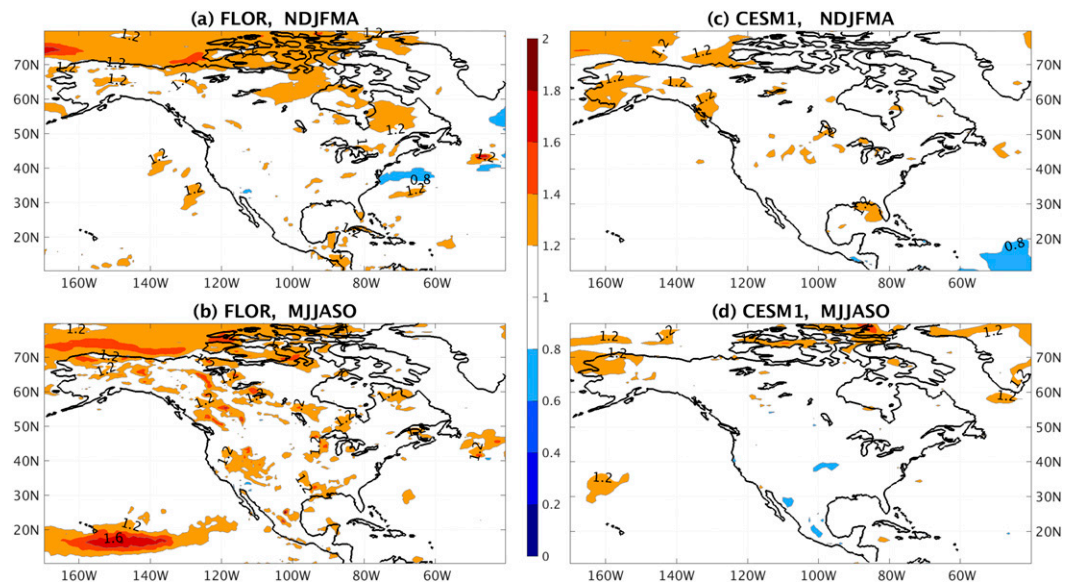


FIG. A1. Ratio of standard deviation of PmE decadal variability during 2000–49 to that in preindustrial control simulation for (a),(c) NDJFMA and (b),(d) MJJASO and for (left) FLOR and (right) CESM1. In control simulations, the standard deviation of PmE decadal variability is computed at each grid point after low-pass filtering PmE time series with a cutoff period of 10 yr; in large ensembles, it is computed at each grid point after 1) subtracting the ensemble mean (forced signal) from each ensemble member, 2) low-pass filtering the remaining PmE time series with a 10-year cutoff period, and 3) concatenating the 2000–50 period of all ensemble members (to form a series of 1750 model years).

North America in MJJASO. Moisture budget analysis is performed to diagnose the physical processes underlying the projected changes in PmE mean state over these regions. Over northeastern North America, projected wintertime moistening changes appear detectable around the 2010s and are attributed to submonthly transient eddies. Submonthly transient eddies can result in the northeastern moistening via the enhanced meridional atmospheric moisture gradient (Seager et al. 2014) in response to global warming and likely also through enhanced eddy activity in this region as a result of the poleward shift and strengthening of the Atlantic storm track (e.g., Yin 2005; Bengtsson et al. 2006; Wu et al. 2011). Over southwestern North America, projected wintertime drying changes appear detectable around the 2000s in FLOR but much later in CESM1, around the 2050s, owing to the larger signal-to-noise ratio in FLOR than in CESM1. Nonetheless, both models simulate a dominant role for monthly mean atmosphere circulation in the projected wintertime drying trend. One possible process from the mean atmospheric circulation is the poleward expansion of tropical Hadley cells in response to greenhouse gas-induced global warming (e.g., Yin 2005; Bengtsson et al. 2006; Lu et al. 2007; Zhang et al. 2016). The descending branch of the Hadley cell expands poleward over southwestern North America, leading to the drying trend (Seager et al. 2007).

Another possible process for the southwestern drying is the northerly dry advection associated with changes in stationary waves (Seager et al. 2014; Simpson et al. 2016). Over central North America, the summertime drying trends appear detectable around the 2000s in both models and are largely explained by a similar drying trend in the diagnosed monthly residual term, which suggests a crucial role of submonthly transient eddies. Although the monthly mean processes diagnosed here mostly show opposite trends between the two models, previous moisture budget analysis based on the 6-hourly CMIP5 model output (Seager et al. 2014) explicitly shows an important role of submonthly transient eddies in the summertime drying trend in this region, corroborating our inference.

Internal climate variability used in the detectability analysis of projected PmE changes is estimated from preindustrial control simulations. Neglecting possible changes in internal climate variability from control to future simulations is estimated to only lead to small errors (<5%; see appendix A) in our results and, therefore, is not considered here. In CESM1, PmE internal climate variability from the atmosphere–land-only control simulation is also used in the detectability analysis. Similar results are found, suggesting that atmosphere–land intrinsic dynamics play a dominant role in the PmE internal climate variability in CESM1. This conclusion

TABLE A1. Fraction (%) of the area where ensemble-mean PmE changes relative to the 1950–99 climate can be attributed to externally forced signal against internal climate variability in fully coupled control simulations during (top) NDJFMA and (bottom) MJJASO, respectively. Numbers inside parentheses indicate the adjusted fraction after rescaling based on ratios shown in Fig. A1.

	GFDL FLOR 35-member RCP4.5 ALLFORC (rescaled)			NCAR CESM1 35-member RCP8.5 ALLFORC (rescaled)		
	Land	Ocean	Total	Land	Ocean	Total
<b>NDJFMA</b>						
2000–09	27.7 (23.8)	35.3 (31.5)	32.9 (29.1)	11.5 (8.3)	23.4 (22.6)	19.1 (17.5)
2010–19	37.5 (33.8)	52.2 (48.6)	47.6 (44.0)	31.6 (27.4)	39.5 (37.1)	36.6 (33.6)
2020–29	46.9 (43.3)	63.5 (60.5)	58.4 (55.1)	50.5 (47.2)	50.3 (48.9)	50.3 (48.4)
2030–39	55.3 (51.5)	71.2 (68.5)	66.3 (63.2)	63.4 (60.9)	63.9 (62.5)	63.7 (62.0)
2040–49	62.7 (59.0)	73.6 (71.6)	70.2 (67.7)	69.8 (67.7)	73.3 (72.1)	72.0 (70.5)
2050–59	—	—	—	78.4 (75.5)	75.2 (72.2)	76.4 (73.4)
2060–69	—	—	—	81.6 (79.2)	79.7 (77.8)	80.4 (78.3)
2070–79	—	—	—	82.8 (80.8)	81.4 (79.5)	81.9 (80.0)
2080–89	—	—	—	86.5 (84.5)	84.8 (83.0)	85.4 (83.6)
2090–99	—	—	—	87.5 (86.0)	87.4 (86.1)	87.4 (86.1)
<b>MJJASO</b>						
2000–09	26.6 (21.8)	27.9 (22.8)	27.5 (22.5)	17.5 (17.2)	23.1 (21.8)	21.1 (20.1)
2010–19	37.2 (31.8)	30.1 (26.1)	32.3 (27.8)	36.1 (35.0)	37.7 (37.3)	37.1 (36.5)
2020–29	49.1 (43.7)	43.0 (38.4)	44.9 (40.0)	52.7 (52.0)	50.2 (48.9)	51.1 (50.0)
2030–39	55.8 (51.7)	47.4 (43.2)	50.0 (45.8)	61.2 (60.7)	60.1 (59.3)	60.5 (59.8)
2040–49	59.7 (54.9)	51.7 (47.9)	54.2 (50.1)	65.8 (65.1)	63.0 (62.1)	64.0 (63.2)
2050–59	—	—	—	72.8 (71.0)	64.9 (63.8)	67.8 (66.4)
2060–69	—	—	—	75.3 (74.3)	71.3 (70.2)	72.7 (71.7)
2070–79	—	—	—	78.7 (77.9)	73.7 (72.4)	75.5 (74.4)
2080–89	—	—	—	80.1 (79.5)	77.0 (74.9)	78.1 (76.5)
2090–99	—	—	—	81.3 (80.7)	81.1 (79.2)	81.2 (79.7)

is consistent with previous findings that uncertainties caused by internal climate variability in future projections are largely attributed to variations of large-scale atmospheric circulation (Deser et al. 2014).

The detectability analysis in CESM1 is further extended to 2050–2100. A main finding is that the spatial pattern of projected changes in PmE mean state remains similar to that by 2050, but the magnitude of the projected PmE changes keeps growing along with the enhanced anthropogenic radiative forcing. This result suggests that the spatial pattern of projected changes in PmE mean state will be largely stabilized before the middle of the current century, with most of North America (>70% in CESM1) projected to experience detectable changes in PmE mean state by 2050.

This work quantitatively illustrates that anthropogenically forced changes in hydroclimate mean state over North America are detectable even on decadal time scales, on which internal climate variability dominates hydroclimate changes. Detectable anthropogenic changes in the hydroclimate mean state are projected over most of North America by 2050. These model results are of importance for climate mitigation and adaptation.

*Acknowledgments.* We thank Salvatore Pascale, Hiroyuki Murakami, and three anonymous reviewers for

insightful and constructive comments on the manuscript. We also thank Gabriel Vecchi and Karen Paffendorf for designing and conducting the FLOR ensembles and thank the CESM Large Ensemble Community Project (<http://www.cesm.ucar.edu/projects/community-projects/LENS/>) and supercomputing resources provided by NSF/CISL/Yellowstone. H. Zhang is supported through Princeton University under block funding from NOAA/GFDL; T. Delworth is supported as a base activity of NOAA/GFDL.

## APPENDIX A

### Comparison of PmE Low-Frequency Internal Variability between Preindustrial Control Simulation and Future Projections

We compare low-frequency internal variability of PmE in preindustrial control simulations with that in future 2000–50 projections and assess the impacts of assuming stationary PmE internal variability in the detectability analysis on our results. In preindustrial control simulations, low-frequency internal variability at each grid point is measured as the standard deviation of low-pass-filtered PmE time series with a 10-yr cutoff period. In the 35-member ALLFORC ensembles, it is measured as the standard deviation of a 1750-yr PmE

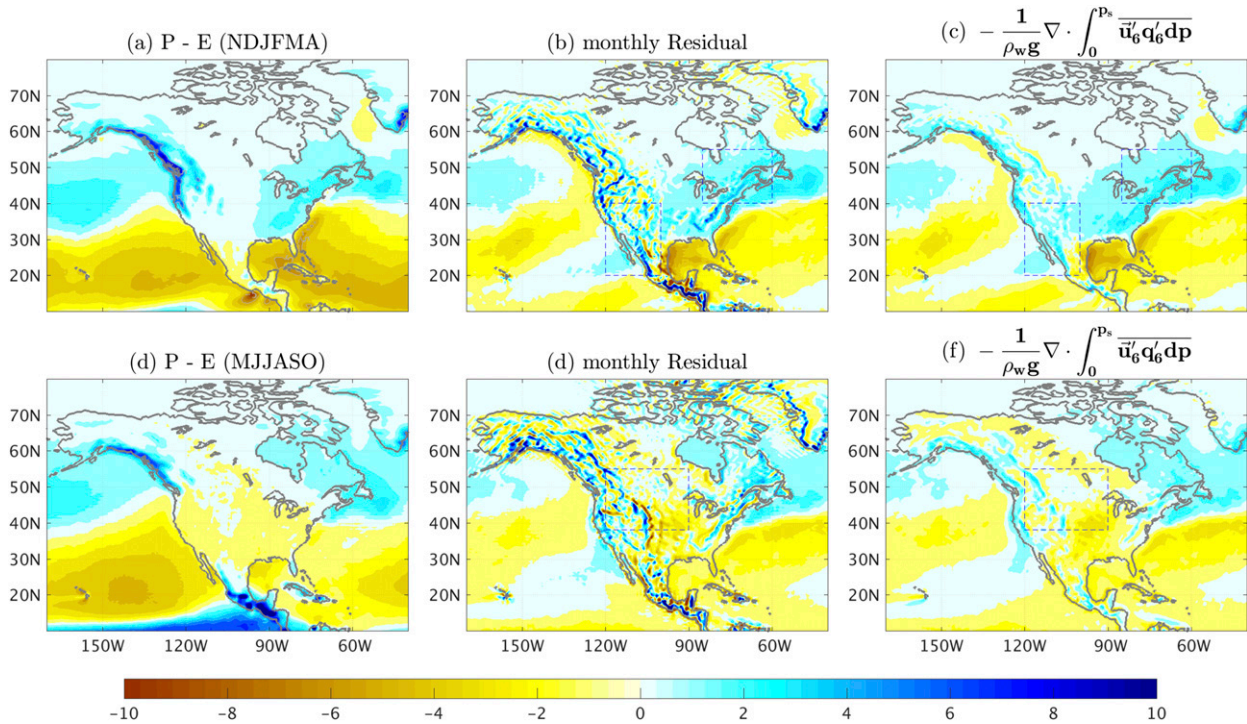


FIG. B1. (a)–(c) Winter (NDJFMA) and (d)–(f) summer (MJJASO) moisture budget ( $\text{mm day}^{-1}$ ) climatology from the 20-yr FLOR control simulation. (left) PmE; (center) budget residual resulted from monthly fields; and (right) moisture flux divergence by submonthly transient eddies computed from 6-hourly fields. [Blue dashed boxes in (center) and (right) indicate the regions where time series of moisture budget terms is computed in Fig. B2.]

series constructed as follows: 1) first subtracting the ensemble mean of PmE time series (forced component) from each ensemble member, 2) then low-pass filtering (10-yr cutoff period) the remaining PmE time series during 1950–2050 in each member, and 3) finally concatenating the 2000–50 period of all 35 members to form the 1750-yr series. The ratio of the PmE standard deviation in ALLFORC ensembles to preindustrial control simulations is shown in Fig. A1 for FLOR and CESM1 in winter and summer, respectively.

From preindustrial-level to future RCP4.5 radiative forcing in FLOR, low-frequency internal variability of PmE in both seasons increases by less than 20% over most of North America, except for polar ocean and summertime subtropical North Pacific and scattered North American land, where the increase is about 20%–60% (mostly below 40%). In CESM1, from preindustrial-level to future RCP8.5 radiative forcing, the increase in low-frequency PmE internal variability is smaller and over fewer regions than in FLOR, and there is a substantial area over subtropical ocean and summertime land where the PmE internal variability decreases by less than 20%.

The increase or decrease in low-frequency PmE internal variability from preindustrial simulations to future

projections implies a possible overestimation or underestimation of the detectability of projected shifts in PmE mean state based on preindustrial-level internal variability. To assess this effect, we perform the detectability analysis by using the range of internal variability rescaled with the ratios shown in Fig. A1 (assuming that the ratios estimated here apply to the internal variability constructed with the Monte Carlo approach in the main text) and find small changes to our results—an overall <5% of overestimation in the fraction of the area, with detectable PmE changes over North America (Table A1). The small effect on our results is because the detectability is based on the signal-to-noise ratio, rather than just on the noise (internal variability). Considering this small effect, we only report results based on the preindustrial-level internal variability.

## APPENDIX B

### Relationship between Submonthly Transient Eddies and Monthly Residual in Moisture Budget Analysis

To demonstrate the dominant role of submonthly transient eddies in the residual of the moisture budget using monthly mean fields, we perform a 20-yr control run

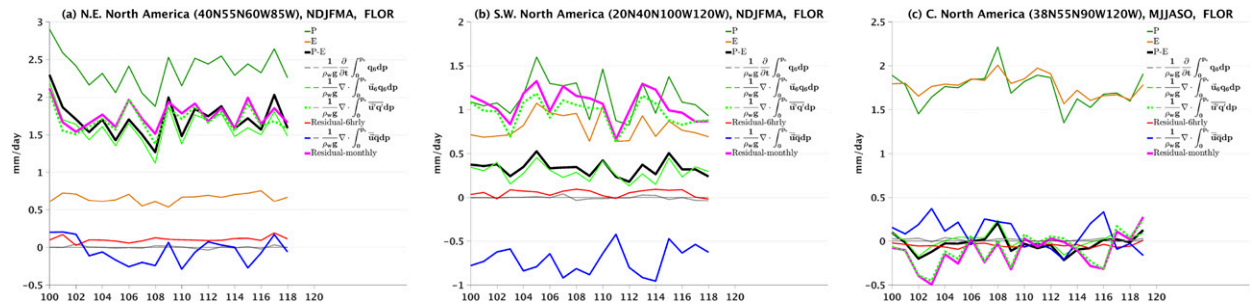


FIG. B2. Time series of moisture budget terms averaged over (a) northeastern and (b) southwestern North America during winter (NDJFMA) and (c) central North America during summer (MJJASO). The three regions are shown in Fig. B1 by the blue dashed boxes in middle and right columns. Note in all three regions, the variation of monthly residual term (magenta curve) follows that of submonthly transient eddies (green dashed curve) resolved by the 6-hourly fields.

with the GFDL FLOR model and save output at both 6-hourly and monthly mean resolutions. Using the overbar to denote the monthly mean, subscript 6 to denote the 6-hourly mean, and prime to denote the departure of 6-hourly fields from their monthly mean, the transient eddy term can be expressed as  $\overline{u'_6 q'_6} = \overline{u_6 q_6} - \overline{u} \overline{q}$ . Moisture budget analysis is carried out with the 6-hourly and monthly mean output separately.

Fig. B1 shows the 20-yr climatology of the moisture budget terms over North America during winter and summer, respectively. The eddy term is large during winter over regions influenced by the Pacific and Atlantic storm tracks (i.e., eastern North Pacific and around the east coast of North America) and during summer, mainly over northeastern North America and surrounding oceans; in these regions, the monthly residual term exhibits very similar features, suggesting the dominant role of submonthly transient eddies in the monthly residual term. This relationship is further supported by the time series of the moisture budget averaged over the three regions that have early detectability of projected PmE changes (recall Figs. 3 and 4). In all three regions (Fig. B2), the interannual variations of the monthly residual term (magenta curve) follow closely the eddy term (dashed green curve). This result suggests that trends appearing in the monthly residual can be attributed to changes in submonthly transient eddies.

## REFERENCES

- Bengtsson, L., K. I. Hodges, and E. Roeckner, 2006: Storm tracks and climate change. *J. Climate*, **19**, 3518–3543, <https://doi.org/10.1175/JCLI3815.1>.
- Branstator, G., H. Teng, G. A. Meehl, M. Kimoto, J. R. Knight, M. Latif, and A. Rosati, 2012: Systematic estimates of initial-value decadal predictability for six AOGCMs. *J. Climate*, **25**, 1827–1846, <https://doi.org/10.1175/JCLI-D-11-00227.1>.
- Delworth, T. L., F. Zeng, A. Rosati, G. A. Vecchi, and A. T. Wittenberg, 2015: A link between the hiatus in global warming and North American drought. *J. Climate*, **28**, 3834–3845, <https://doi.org/10.1175/JCLI-D-14-00616.1>.
- Deser, C., R. Knutti, S. Solomon, and A. S. Phillips, 2012: Communication of the role of natural variability in future North American climate. *Nat. Climate Change*, **2**, 775–779, <https://doi.org/10.1038/nclimate1562>.
- , A. S. Phillips, M. A. Alexander, and B. V. Smoliak, 2014: Projecting North American climate over the next 50 years: Uncertainty due to internal variability. *J. Climate*, **27**, 2271–2296, <https://doi.org/10.1175/JCLI-D-13-00451.1>.
- Harris, I., P. D. Jones, T. J. Osborn, and D. H. Lister, 2014: Updated high-resolution grids of monthly climatic observations—The CRU TS3.10 dataset. *Int. J. Climatol.*, **34**, 623–642, <https://doi.org/10.1002/joc.3711>.
- He, J., C. Deser, and B. J. Soden, 2017: Atmospheric and oceanic origins of tropical precipitation variability. *J. Climate*, **30**, 3197–3217, <https://doi.org/10.1175/JCLI-D-16-0714.1>.
- Held, I. M., and B. J. Soden, 2006: Robust responses of the hydrological cycle to global warming. *J. Climate*, **19**, 5686–5699, <https://doi.org/10.1175/JCLI3990.1>.
- Hoerling, M., and Coauthors, 2011: On North American decadal climate for 2011–20. *J. Climate*, **24**, 4519–4528, <https://doi.org/10.1175/2011JCLI4137.1>.
- Hurrell, J. W., and Coauthors, 2013: The Community Earth System Model: A framework for collaborative research. *Bull. Amer. Meteor. Soc.*, **94**, 1339–1360, <https://doi.org/10.1175/BAMS-D-12-00121.1>.
- IPCC, 2013: *Climate Change 2013: The Physical Science Basis*. Cambridge University Press, 1535 pp., <https://doi.org/10.1017/CBO9781107415324>.
- Kay, J. E., and Coauthors, 2015: The Community Earth System Model (CESM) Large Ensemble project: A community resource for studying climate change in the presence of internal climate variability. *Bull. Amer. Meteor. Soc.*, **96**, 1333–1349, <https://doi.org/10.1175/BAMS-D-13-00255.1>.
- Kirtman, B., and Coauthors, 2013: Near-term climate change: Projections and predictability. *Climate Change 2013: The Physical Science Basis*, T. F. Stocker et al., Eds., Cambridge University Press, 953–1028, <https://doi.org/10.1017/CBO9781107415324.023>.
- Lehner, F., S. Coats, T. F. Stocker, A. G. Pendergrass, B. M. Sanderson, C. C. Raible, and J. E. Smerdon, 2017: Projected drought risk in 1.5°C and 2°C warmer climates. *Geophys. Res. Lett.*, **44**, 7419–7428, <https://doi.org/10.1002/2017GL074117>.
- Lin, L., A. Gettelman, Q. Fu, and Y. Xu, 2016: Simulated differences in 21st century aridity due to different scenarios of

- greenhouse gases and aerosols. *Climatic Change*, <https://doi.org/10.1007/s10584-016-1615-3>, in press.
- Lu, J., G. A. Vecchi, and T. Reichler, 2007: Expansion of the Hadley cell under global warming. *Geophys. Res. Lett.*, **34**, L06805, <https://doi.org/10.1029/2006GL028443>.
- Maloney, E. D., and Coauthors, 2014: North American climate in CMIP5 experiments: Part III: Assessment of twenty-first-century projections. *J. Climate*, **27**, 2230–2270, <https://doi.org/10.1175/JCLI-D-13-00273.1>.
- Meinshausen, M., and Coauthors, 2011: The RCP greenhouse gas concentrations and their extensions from 1765 to 2300. *Climatic Change*, **109**, 213–241, <https://doi.org/10.1007/s10584-011-0156-z>.
- Neelin, J. D., B. Langenbrunner, J. E. Meyerson, A. Hall, and N. Berg, 2013: California winter precipitation change under global warming in the Coupled Model Intercomparison Project phase 5 ensemble. *J. Climate*, **26**, 6238–6256, <https://doi.org/10.1175/JCLI-D-12-00514.1>.
- Sanderson, B. M., K. W. Oleson, W. G. Strand, F. Lehner, and B. C. O'Neill, 2015: A new ensemble of GCM simulations to assess avoided impacts in a climate mitigation scenario. *Climatic Change*, <https://doi.org/10.1007/s10584-015-1567-z>, in press.
- Sarojini, B. B., P. A. Stott, and E. Black, 2016: Detection and attribution of human influence on regional precipitation. *Nat. Climate Change*, **6**, 669–675, <https://doi.org/10.1038/nclimate2976>.
- Schneider, U., A. Becker, P. Finger, A. Meyer-Christoffer, B. Rudolf, and M. Ziese, 2011: GPCC Full Data Reanalysis version 6.0 at 0.5°: Monthly land-surface precipitation from rain-gauges built on GTS-based and historic data. GPCC, accessed June 2017, <https://www.esrl.noaa.gov/psd/data/gridded/data.gpcc.html>.
- Seager, R., and N. Henderson, 2013: Diagnostic computation of moisture budgets in the ERA-Interim reanalysis with reference to analysis of CMIP-archived atmospheric model data. *J. Climate*, **26**, 7876–7901, <https://doi.org/10.1175/JCLI-D-13-00018.1>.
- , and Coauthors, 2007: Model projections of an imminent transition to a more arid climate in southwestern North America. *Science*, **316**, 1181–1184, <https://doi.org/10.1126/science.1139601>.
- , and Coauthors, 2014: Dynamical and thermodynamical causes of large-scale changes in the hydrological cycle over North America in response to global warming. *J. Climate*, **27**, 7921–7948, <https://doi.org/10.1175/JCLI-D-14-00153.1>.
- Simpson, I. R., R. Seager, M. Ting, and T. A. Shaw, 2016: Causes of change in Northern Hemisphere winter meridional winds and regional hydroclimate. *Nat. Climate Change*, **6**, 65–70, <https://doi.org/10.1038/nclimate2783>.
- Smith, D. M., S. Cusack, A. W. Colman, C. K. Folland, G. R. Harris, and J. M. Murphy, 2007: Improved surface temperature prediction for the coming decade from a global climate model. *Science*, **317**, 796–799, <https://doi.org/10.1126/science.1139540>.
- Vecchi, G. A., and Coauthors, 2014: On the seasonal forecasting of regional tropical cyclone activity. *J. Climate*, **27**, 7994–8016, <https://doi.org/10.1175/JCLI-D-14-00158.1>.
- Wallace, J. M., C. Deser, B. V. Smoliak, and A. S. Phillips, 2015: Attribution of climate change in the presence of internal variability. *Climate Change: Multidecadal and Beyond*, C.-P. Chang et al., Eds., World Scientific, 1–29, [https://doi.org/10.1142/9789814579933\\_0001](https://doi.org/10.1142/9789814579933_0001).
- Wu, Y., M. Ting, R. Seager, H.-P. Huang, and M. A. Cane, 2011: Changes in storm tracks and energy transports in a warmer climate simulated by the GFDL CM2.1 model. *Climate Dyn.*, **37**, 53–72, <https://doi.org/10.1007/s00382-010-0776-4>.
- Xie, S.-P., and Coauthors, 2015: Towards predictive understanding of regional climate change. *Nat. Climate Change*, **5**, 921–930, <https://doi.org/10.1038/nclimate2689>.
- Yang, X., and Coauthors, 2013: A predictable AMO-like pattern in the GFDL fully coupled ensemble initialization and decadal forecasting system. *J. Climate*, **26**, 650–661, <https://doi.org/10.1175/JCLI-D-12-00231.1>.
- Yin, J. H., 2005: A consistent poleward shift of the storm tracks in simulations of 21st century climate. *Geophys. Res. Lett.*, **32**, L18701, <https://doi.org/10.1029/2005GL023684>.
- Zhang, H., T. Delworth, F. Zeng, G. Vecchi, K. Paffendorf, and L. Jia, 2016: Detection, attribution, and projection of regional rainfall changes on (multi-) decadal time scales: A focus on southeastern South America. *J. Climate*, **29**, 8515–8534, <https://doi.org/10.1175/JCLI-D-16-0287.1>.